atmosphere

Article

Numerical Simulation of Charge Structure Evolution during the Feeder-Type Cells Merging

Jie Deng [1], Fengxia Guo [1,*], Jing Sun [2], Zeyi Wu [1], Zhou Liu [1], Xian Lu [1], Ke Chen [1] and Qingyuan Wang [1]

[1] Emergency Management College/Collaborative Innovation Center on Forecast and Evaluation of Meteorological Disasters (CIC-FEMD), Nanjing University of Information Science & Technology, Nanjing 210044, China; dj112355@163.com (J.D.); wzeey97@163.com (Z.W.); liuzhou980@gmail.com (Z.L.); luxiannuist@163.com (X.L.); 19850066613@139.com (K.C.); wqy000301@163.com (Q.W.)

[2] Hubei Key Laboratory for Heavy Rain Monitoring and Warning Research, Institute of Heavy Rain, China Meteorological Administration, Wuhan 430205, China; sunjing@whihr.com.cn

* Correspondence: guofx@nuist.edu.cn

Abstract: Formation of the multipolar charge structure during feeder-type cell merging has important consequences in severe convective weather. This study used the Weather Research and Forecasting model with electrification and discharge parameterization schemes to simulate the feeder-type cell merging process in the tail of a squall line that occurred on 27 June 2020 in Hubei Province (China). The results showed that the two cells involved in the merging process were at different life stages, but that the distribution of the inductive charging zones in the parent and child cells was broadly the same as that of the non-inductive charging zones. The charging zones were restricted to the mixed-phase region (between the 0 and −40 °C layers) with a cloud water content of >0.2 g/kg in the updraft zone, and the magnitude of the inductive charging rate was slightly smaller than that of the non-inductive charging rate. The differences in the vertical wind shear between the parent and child cells caused differences in the content, charge number, and polarity of the hydrometeors, which resulted in obvious differences in the charge structure characteristics between the two cells. Overall, the cloud droplets, ice, snow, and graupel were the main charged hydrometeors in the cells, whereas the rain and hail had little charge.

Keywords: numerical simulation; cells merger; charge structure; electrification; hydrometeor

Citation: Deng, J.; Guo, F.; Sun, J.; Wu, Z.; Liu, Z.; Lu, X.; Chen, K.; Wang, Q. Numerical Simulation of Charge Structure Evolution during the Feeder-Type Cells Merging. *Atmosphere* **2023**, *14*, 1588. https://doi.org/10.3390/atmos14101588

Academic Editors: Richard Müller, Feifei Shen and Yunheng Wang

Received: 9 August 2023
Revised: 14 October 2023
Accepted: 18 October 2023
Published: 20 October 2023

1. Introduction

Mesoscale severe convective weather systems typically undergo a multistage cell merging process [1–5]. The concept of cells merging was proposed in the 1950s but a standardized definition remains lacking. Tao et al. [6] considered the first consolidation of two or more mutually independent cells at the 1 mm/h isopleth of the rain rate as the beginning of a merger, whereas Kogan et al. [7] regarded the formation of a single closed circuit of maximum vertical velocity of neighboring isolated convective cells in the horizontal cross-section of an updraft at a certain altitude as cells merging. Lee et al. [8] defined cells merging as the strongest echo cores of two independent cells overlapping at the minimum radar elevation angle (0.5°). Gauthier et al. [9] defined a convective cell as a continuous region with composite reflectivity (CR) ≥ 30 dBZ. On that basis, some studies regarded the aggregation of neighboring echoes with CR ≥ 30 dBZ as the beginning of cells merging, whereas strong echo cores with CR > 45 dBZ that were merged into a continuous compact region were regarded as indicative of the completion of cells merging [10–12].

Cells merging can take various forms. Differences in the conditions of merging cells and merger types might be due to differences in the merging mechanism [13–18]. On the basis of plan position indicator radar data, Wang et al. [19] concluded that five types of cell merger can occur during the evolution of hail clouds: swallowing, jetting, finger-shaped, chasing, and convergence mergers. Through analysis of radar data showing cell merging processes in a multicell hailstorm, Yi et al. [20] found two merger types in γ mesoscale cells or small β mesoscale convective cells: independent and feeder-type merging. The independent merger occurred between two cells that differed in terms of their time of formation and intensity. The feeder-type merger occurred when a warm moist air mass in front of a mature cell was lifted by a downdraft from the older cell, leading to the generation of a new cell. In this circumstance, the mature cell is known as the parent cell, and the new cell is known as the child cell. The two cells were in different life stages. The divergent outflow from the upper part of the parent cell provided a dynamic background favorable for stimulating the generation of the child cell. Moreover, the precipitation from the parent cell created humid conditions for the child cell, which promoted strong growth of the child cell while the parent cell gradually weakened, and the strong echo cores tended to gradually merge. This process is consistent with the concept of a feeder-type cell merger proposed by Dennis et al. [21]. Yi et al. [18] found that feeding and swallowing relationships exist for mergers between cells and β mesoscale cells in a linear mesoscale convective system (LL-MCS). After the cell merges with the LL-MCS, the cell continues to develop and finally integrates into the LL-MCS, which is similar to the feeder-type merger proposed by both Yi et al. [20] and Dennis et al. [21].

The cells merging process affects the developmental characteristics of the dynamical and microphysical fields, which in turn affect the electrification process, charge structure, and lightning activity of thunderstorms [22–26]. Yi et al. [10] selected 23 cell merging processes, 10 of which included lightning activity, and analyzed the associated S-band Doppler radar data and Safir3000 lightning localization system data. It was found that during 97% of the mergers, the volume with echo intensity > 40 dBZ at altitude > 6 km and the volume with echo intensity > 40 dBZ showed an increasing trend, and that the lightning frequency of nine samples jumped or even peaked. It suggests that cells merging strengthened the updrafts and the water vapor transition, forming ice-phase particles and supercooled water droplets of sufficient size and quantity conducive to the occurrence of lightning. During the merging process, the downdraft interacted with the updraft, which weakened the updraft for a short period, causing the height of the main zone of the positive charge to drop by 1–4 km. Then, the updraft recovered after 6–12 min, and the main zone of the positive charge returned to its original height. Lu et al. [11] analyzed three feeder-type cell merging processes using Beijing Broadband Lightning Location Network and S-band Doppler radar data. They found that after the process of merging began, the convergence in the bottom part of the front cell caused the transport of water vapor from the cell base to the upper part of the cloud, forming abundant ice-phase particles in the mixed-phase region, which favored the occurrence of non-inductive charging and generated lightning. Lu et al. [12] used the WRF model to simulate a severe squall line that occurred over the Beijing metropolitan region. The squall line involved merger processes between multiple γ and β mesoscale cells, which formed the main LL-MCS. Their results showed that the squall line had an overall normal tripolar "positive–negative–positive" (hereafter, P–N–P) charge structure during the early stage of multiple isolated cells. During the approach to the merger of the main band, the main band of convection showed a bipolar N–P vertical charge structure. After the merger between the main convective cells began, the overall vertical charge structure evolved into a uniformly distributed five-layer structure (i.e., P–N–P–N–P). From the near-ground region to the cloud top, the distribution of the charge region widened, the charge density increased, the spacing between the charge layers decreased, and the increasing vertical electric field led to an increased frequency of lightning during the merging period.

In summary, diverse types of cell merging occur in severe convective weather. The different types of cell merger with different merging mechanisms have different impacts on the dynamics, microphysical processes, and electrical processes of convective clouds. However, few studies have investigated the type of cell merging processes, and the cognitions of feeder-type cells merging are based on the observation results, such as the convective development and structural changes of cells during the feeder-type cells merging, which were both inferred inversely based on radar parameters, and the evolutionary characteristics of the main positive charge zone during the feeder-type cells merging were inferred inversely based on the data from the Safir3000 lightning radiation. None of the above methods can reproduce the overall charge structure and the evolution of the distribution of hydrometeors in the cell, not to mention the spatial evolution characteristics of the cloud electrification process.

This study used radar observation data and the WRF model with electrification and discharge parameterization schemes to investigate the feeder-type cells merging process that occurred in the tail of a squall line over Jingmen (Hubei Province, China). We analyzed the relationships between the changes in the dynamical–microphysical processes and the characteristics of the evolution of the charge structure, updrafts, and charging regions in the cloud before and after the feeder-type cells merging. The objective was to improve our understanding of the characteristics of the evolution of the charge structure and its causes during the feeder-type cells merging process.

2. Synoptic Conditions and Model Settings

2.1. Synoptic Conditions

On 27–28 June 2020, a synoptic situation comprising two ridges and a trough in the high latitudes of Eurasia produced a strong southwest–northeast jet stream in the middle and low layers over China, with conditions of high humidity and strong vertical wind shear. Satellites and radar both observed the development of a southwest–northeast-trending MCS over parts of central China, accompanied by localized short-term heavy precipitation, thunderstorms, gales, and other severe convective weather.

Satellite imagery indicated that two α mesoscale convective clouds merged over Jingmen (Hubei Province) at 11:00 (all times UTC) on 27 June 2020, forming a southwest–northeast-trending squall line, with a minimum infrared brightness temperature of 196.77 K. The radar observations of the squall line showed echo intensities of up to 55 dBZ, the tilting of the storm in the vertical direction, and strong echoes ($\geq$45 dBZ) up to the altitude of approximately 7 km. The radar radial velocities indicated the repeated presence of tornado vortexes and mesocyclones, and showed that the lower levels of the storm presented a hook-shaped echo. The field investigation revealed that a tornado appeared at 11:00 on the 27 June in Duodao District, Jingmen City; the duration of the gale was approximately 30 min with a maximum instantaneous wind speed of up to 29.4 m/s, and that the peak rainfall intensity was 71 mm/h at 12:00. According to observations [27], the entire layer of the squall line had a high effective liquid water content, the dew point temperature at 850 hPa was 18 °C, the specific humidity reached 15.3 g/kg, and the wet layer extended out to the vicinity of 400 hPa, representing conditions favorable for both the electrification of the thunderstorm clouds and the occurrence of heavy precipitation. Moderate-intensity wind shear was also conducive to the development of thunderstorm cloud organization, prompting the generation, collision, separation, and electrification of the hydrometeors within the clouds.

2.2. Model Introduction

The NCEP FNL 0.25° $\times$ 0.25° 6 h reanalysis data for a 6 h period starting at 06:00 on 27 June 2020 were used as initial boundary conditions in this study. The simulation area (Figure 1) was dual-nested, consisting of outer (d01) and inner (d02) domains with spatial resolutions of 9 and 1.8 km, respectively. The corresponding horizontal grid dimensions were 145 $\times$ 138, 406 $\times$ 396, with time steps set to 18 and 3.6 s. There were 32 vertical layers, with the top layer at 50 hPa. The long-wave radiation was represented by the Rapid Radiative Transfer Model (RRTM) and the land surface was obtained using the Noah Land Surface Model. The remaining parameterization scheme settings are detailed in Table 1.

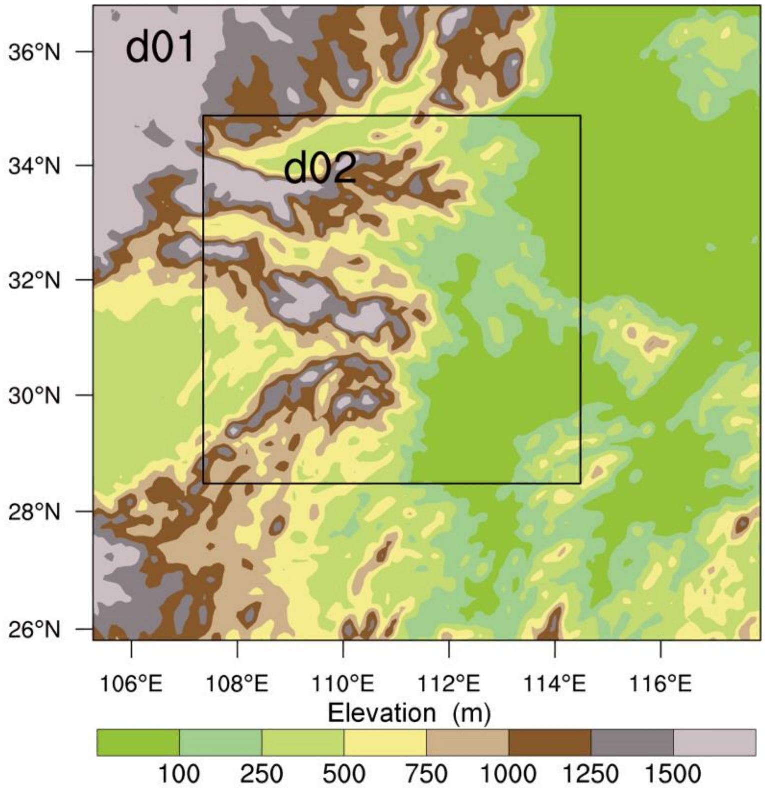

Figure 1. Simulation domain and the distribution of elevation (m).

Table 1. WRF Configuration.

Options	d01	d02
Lattice number	145 × 138	406 × 396
Horizontal resolution	9 km	1.8 km
Time steps	18 s	3.6 s
Microphysics	nssl_2momlgtmsz	nssl_2momlgtmsz
Cumulus parameterization	None	None
Long wave radiation	RRTM	RRTM
Short wave radiation	Dudhia	Dudhia
Boundary layer	Bougeault and Lacarrere (BouLac) TKE	Bougeault and Lacarrere (BouLac) TKE
Land surface	Noah Land Surface Model	Noah Land Surface Model

The three-dimensional compressible nonhydrostatic WRF model (version 3.3.1) is a mesoscale numerical weather prediction system, coupled with the NSSL 2-moment 6-class bulk microphysical scheme. The six bulk species are rain, cloud water, cloud ice, snow, graupel, and hail [28,29]. The NSSL 2-moment 6-class bulk microphysical scheme considers numerous microphysical processes such as the nucleation of ice crystals, freezing of cloud droplets, collection of ice crystals, aggregation of ice crystals, melting of snowflakes, evaporation of water vapor, and condensation. The non-inductive charging process [30–34] is generally recognized as the dominant process of electrification in thunderstorms. In this study, the non-inductive charging scheme obtained by Helsdon et al. [35], based on improved results from the cloud chamber experiments by Saunders et al. [36], referred to as S91, which was coupled with the WRF model to consider the collision and separation of graupel/hail (large ice-phase particles) and ice crystals/snow (small ice-phase particles). The non-inductive charge separation equations refer to Mansell et al. [37]. The model used in this study also incorporated the inductive charging scheme proposed by Ziegler et al. [38]. Owing to their short duration, ice–ice particle collisions generate only a small amount of charge. Therefore, our study primarily considered the inductive collisions between graupel/hail and cloud droplets. The discharge module applied the improved overall discharge parameterization scheme of MacGorman et al. [39], and the flash initiation was based on the runaway breakdown theory, which means that the initial threshold of flash discharge varied with the altitude.

3. Simulation Results

3.1. Validation of Simulation Results and Selection of Research Subjects

Figure 2 shows the CR observed by the S-band WSR-88D Doppler networked radar in Hubei Province on 27 June 2020. At 11:06, there was a bow echo with a length of 264 km near Jingmen, which was moving slowly from the southwest toward the northeast. The strongest echo was up to 55 dBZ. At 11:42, the strong echo area was mainly distributed in the northeast and southwest of the squall line system.

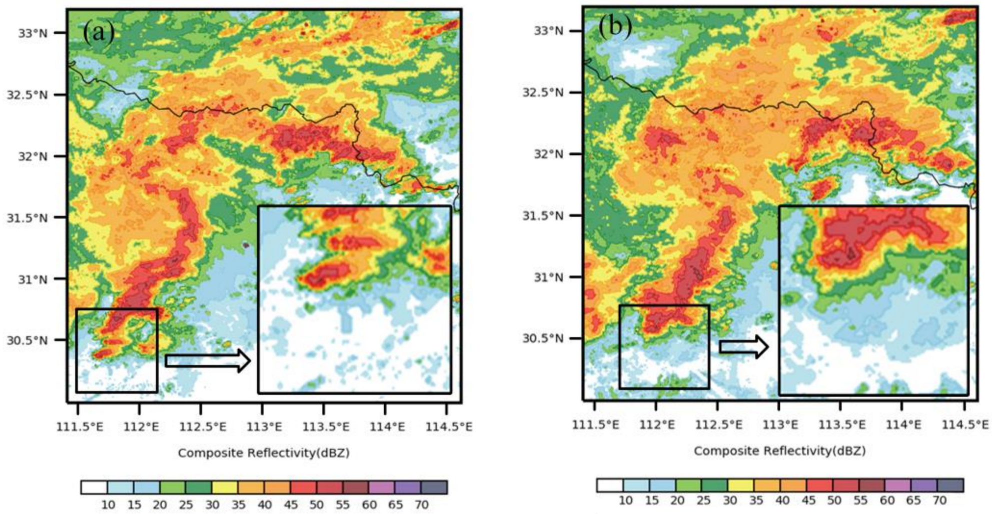

Figure 2. CR was observed by the S-band WSR-88D Doppler networked radar in Hubei Province on 27 June 2020 (example of merger is indicated by the lower left black frame, and the lower right black frame is an enlargement of the lower left black frame). ((**a**). 11:06, start of merger, (**b**). 11:42, end of merger).

A comparison of Figures 2 and 3 reveals certain temporal and spatial biases between the simulation results and the observations. Temporally, the simulated convection occurred approximately 120 min earlier than observed; spatially, the simulated strong echo region was larger and further westward than observed. However, the distributional characteristics of the simulated CR, the maximum echo value, and the trend of movement were similar to the observations. The squall line resulted in the short-term heavy rainfall observed in the local region, and the simulated strong echo was maintained within the local area, broadly matching the observed radar echo. The map of the spatial distribution of the 6 h cumulative precipitation shows that the position of the simulated rain belt was reasonably consistent with that observed, showing a band with a southwest–northeast distribution, and that the simulated center of the maximum precipitation also corresponded well with that observed (figure omitted). Overall, it was considered that the WRF model could simulate the macroscale and microscale characteristics of the studied squall line well, with a certain reproducibility of the underlying processes.

The observations indicate that the squall line experienced a multistage and multiscale merger process. At 11:00, as shown in the black frame in Figure 2, there were two isolated cells at the southwestern tail of the squall line, with clear echo boundaries and with a single continuous strong echo core region. These cells moved northeastward together (figure omitted). At 11:06, the 30 dBZ reflectivity boundaries of the two cells combined for the first time, suggesting that the process of merging had begun (Figure 2a). At 11:42, the strong echo core of the northern cell almost dispersed, while that of the southern cell became vigorous, indicating that the cells merging had finished (Figure 2b).

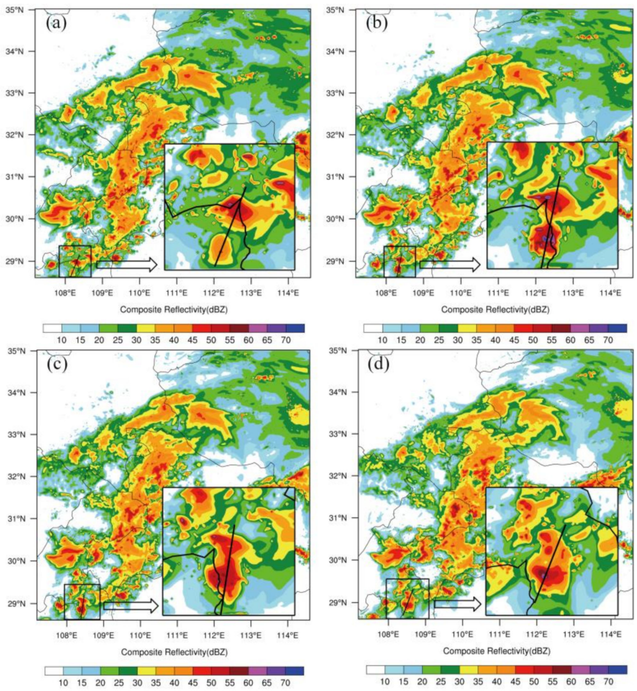

Figure 3. CR simulated by WRF (the lower left black frame is labeled as an example of cell merger under study, the lower right black frame is a magnification of the lower left black frame, and the black line is the location where the vertical profile was selected). ((**a**). 8:54, before the merger, (**b**). 9:00, merger start, (**c**). 9:12, middle of merger, (**d**). 9:36, merger end).

As shown in the black frame in Figure 3, the model also simulated the merger of two mutually independent cells at the southwestern tail of the squall line during 09:00–09:36. Before the merger, the northern cell was in the mature stage, there was a newborn cell to its southwest, and the two cells were moving together toward the northeast (Figure 3a). At the beginning of the merging process, the newborn cell entered the mature stage with its echo core intensity exceeding 55 dBZ, i.e., a value similar to that of the old cell, while the old cell tended to weaken (Figure 3b). In the middle stage of the merger, the convection in the newborn cell became vigorous, while that of the old cell continued to weaken, as evidenced by the reduction in the distributional range of the strong echo core (Figure 3c). At the end of the merger, the old cell dissipated and the newborn cell developed to the mature stage (Figure 3d). This sequence is typical of the feeder-type cell merger process proposed by Yi et al. [18,20], in which the old cell is called the parent cell and the newborn cell is called the child cell. In a feeder-type cell merger process, a child cell is excited near a parent cell, and the parent cell merges with the child cell. Under the effect of the parent cell feeding on the child cell, the convection of the child cell is intensified, while that of the parent cell dissipates, and the strong echo centers of the two cells merge into a single center. In this study, this feeder-type cell merger process was investigated to characterize the microphysical, dynamical, and electrical processes of such convective systems before and after the merging process.

3.2. Characterization of the Evolution of the Echo Intensity, Flow Field, and Spatial Structure of Charge during the Merger

Before the merger, the 30 dBZ echo isopleths of the parent and child cells were not fused. The parent cell (right side) was in the mature stage with a stronger wind shear, and the airflow was mainly divergent to the southwest at the top of the updraft zone, which made the cloud body tilt slightly toward the southwest. The divergent outflow at the cloud top caused a low-level convergence to its southwest, which inspired the generation of the child cell (left side) approximately 10 km to the southwest of the parent cell (Figure 4a). This sequence is consistent with that proposed by Yi et al. [20], whereby the parent cell provides the dynamical background for the development of the child cell in the feeder-type cells merging process.

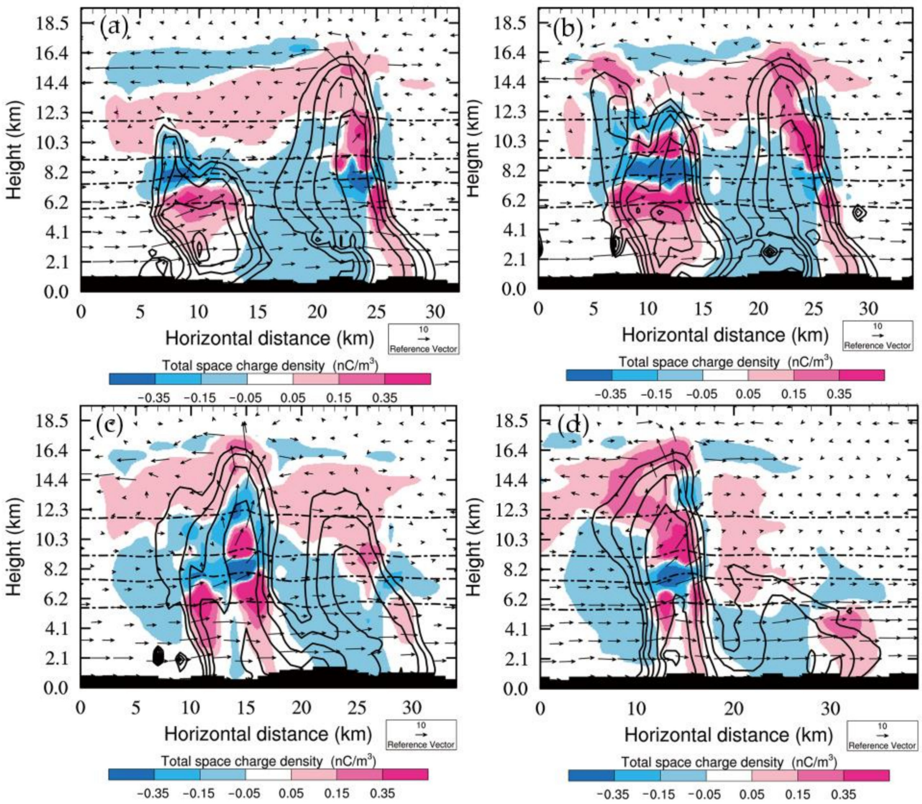

Figure 4. Evolution of the total space charge density (color shaded plot in nC/m^3, which is the sum of all the individual small ions and charged hydrometeors in merging process), flow field (vector arrows in m/s, superimposed horizontal and vertical wind speeds), echo intensity (black isopleths are CR, with values of 30, 36, 42, 48, 54, 60, and 66 dBZ from the outside to the inside, respectively), and the isotherms distribution (black dashed lines are 0, −10, −20, and −40 °C from bottom to top, respectively) along the profile where the black profile line is located at the corresponding moment in Figure 3. ((**a**). 8:54, (**b**). 9:00, (**c**). 9:12, (**d**). 9:36).

At the beginning of the merging process, the parent cell was still strong, the convection of the child cell developed rapidly, and the top altitude of the 30 dBZ echo of the child cell was equal to that of the parent cell. The horizontal pressure gradient force brought the lower parts of the two cells closer, and their 30 dBZ echoes ultimately connected to form a cloud bridge that extended from the ground to the altitude of approximately 3 km (Figure 4b). In the middle of the merging process, the convection of the parent cell weakened and began to dissipate, and the top altitude of the 30 dBZ echo decreased substantially. Simultaneously, the convection of the child cell continued to strengthen, with the top altitude of the 30 dBZ echo exceeding that of the parent cell, the wind shear was weaker, and the cloud bridge altitude lifted to approximately 5 km (Figure 4c). At the end of the merging process, the parent cell dissipated, the top altitude of the 30 dBZ echo of the child cell decreased slightly, and the top altitude of the cloud bridge echo decreased to 3 km (Figure 4d).

The charge density is the sum of all the individual small ions and charged hydrometeors in a volume of per cubic meter. Before the merger, the updraft zone of the parent cell showed a slightly tilted tripolar (P–N–P) charge structure. The periphery of the updraft zone of the parent cell (i.e., the region between the two cells) had a lower negative, middle positive, and upper negative (N–P–N) charge structure, which was distributed over a more uniformly vertical extent and with a lower charge density, the lower two charge regions were thicker and the top negative charge region was thinner. The child cell exhibited a bipolar charge structure, where the upper positive charge region had not formed (P–N), and where the density and extent of the lower positive charge region were comparable to those of the main negative charge region. The negative and main positive charge zones at the cloud anvil of the parent cell were transported to the top of the child cell by the horizontal airflow (Figure 4a).

At the beginning of the merging process, the charge structure of the internal and external regions of the updraft zone of the parent cell remained largely unchanged. However, within the updraft zone, the charge density in the main positive charge region was enhanced, whereas that in the main negative and secondary positive charge regions was weakened. The charge structure of the updraft zone of the child cell showed a six-layer (P–N–P–N–P–N) charge structure with a relatively uniform distribution in the vertical direction. However, the charge density of the main negative and secondary positive charge regions increased, and the distributional range of the secondary positive charge regions expanded (Figure 4b).

A comparison of Figure 4c,d reveals that from the middle to late period of the merging process, the overall characteristics of the charge structure in the updraft zone of the parent cell were broadly similar to those before, except that the overall height of each charge region of the parent cell decreased, the charge density gradually weakened, and the main positive charge region gradually disappeared. The thin layer with negative charge, previously located in the upper part of the updraft zone of the child cell, was transported to the cloud anvil by the horizontal outflow, such that the updraft zone of the child cell developed a five-layer (P–N–P–N–P) charge structure. The strong airflow disrupted the continuity of the charge regions, causing the upper positive and upper negative charge regions to gradually fragment. The extent of the charge region in the periphery of the parent cell updraft zone diminished and the charge density weakened. The charge structure features similar to those detected at the periphery of the parent cell updraft zone were also seen at the periphery of the child cell updraft zone.

3.3. Distribution and Charging Characteristics of Hydrometeors before the Merger

Figure 5 shows the distributional characteristics of the hydrometeors before the merging process. At this time, the parent cell was in the mature stage, and a strong maximum updraft appeared in the middle and upper parts of the cumulus cloud. Conversely, the child cell was in the development stage, the maximum updraft was smaller, and its position was lower.

The content of the ice-phase particles of the child cell was relatively low. The horizontal scale, vertical thickness, altitudes reached, and the central values of the number concentration and the mixing ratio of the region in which the ice-phase particles of the parent cell were located were much greater than those of the child cell, providing conditions favorable for the non-inductive charging process within the parent cell. The −40 to −20 °C mixed-phase region had ample supercooled droplets, coexistent ice and snow, and severe convection conducive to the formation of microphysical processes of snow, e.g., ice crystal collection and aggregation, ice and snow crystal diffusion and depositional growth, and snow crystal riming. The distribution of the snow was similar to that of the ice; however, because the size of the region of snow was larger than that of the ice, the distribution center was located in the lower part of the ice region. The snow further rimed to form graupel, the scale of which was larger than the snow; therefore, the center of the graupel distribution was beneath the snow region, and the graupel continued to rime and form hail. The graupel mixing ratio of the parent cell was separated from the center of its number concentration, indicating that larger hail formed at this time. There was a severe horizontal flow at the anvil of the parent cell cloud toward the child cell, transporting large quantities of ice and snow horizontally from the upper-middle part of the updraft zone of the parent cell to the upper part of the child cell.

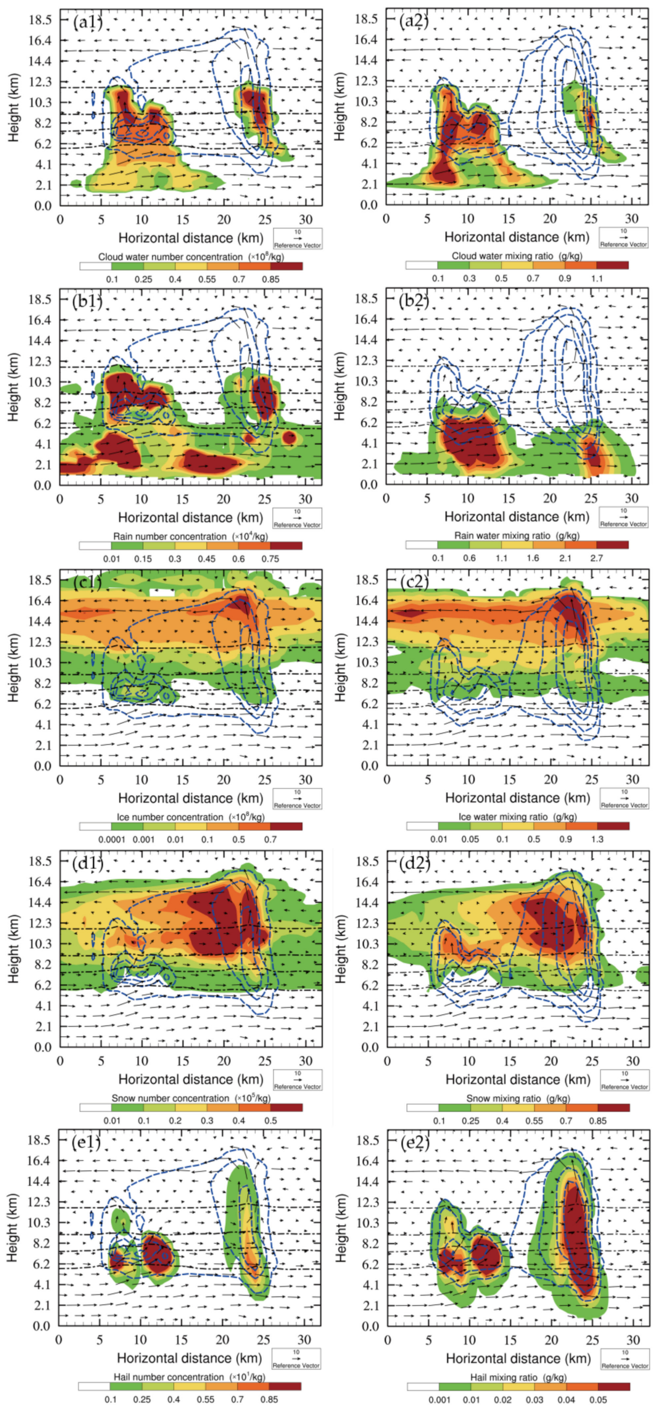

Figure 5. At 8:54, the number concentration (**a1**–**e1**) and mixing ratio (**a2**–**e2**) of hydrometeors, flow field (vector arrows in m/s, superimposed horizontal and vertical wind speeds), number concentration of graupel (blue dashed isopleths in the left column are 0.1, 0.7, 1.3, 1.9, and 2.5 ($\times 10^3$/kg) from the outside to the inside, respectively), mixing ratio of graupel (blue dashed isopleths in the right column are 0.1, 0.5, 2.0, and 3.5 g/kg from the outside to the inside, respectively), and isotherms distribution (black dashed lines are 0, −10, −20, and −40 °C from bottom to top, respectively) along the profile shown by the black profile line in Figure 3a. ((**a**). Cloud, (**b**). rain, (**c**). ice, (**d**). snow, (**e**). hail).

At this time, the supply of warm and humid air to the parent cell was cut off. The cloud droplets were consumed in large quantities through the Bergeron and riming processes, and the cloud droplet distribution zone was small and mainly within the updraft zone between the 0 and −40 °C layers. The center of the number concentration of rain water was consistent with that of the cloud droplets, but the center of the rain water mixing ratio was distributed between the ground and the 0 °C layer with a small value, indicating that it was in the late precipitation stage at this time. The altitude range of the center of the number concentration of both the cloud water and rain water in the child cell was the same as that in the parent cell. However, owing to its constant supply of warm and humid air, there were few ice-phase particles in the child cell and less liquid water was consumed. Therefore, the ranges of the large-value zones of the number concentrations and mixing ratios of both the cloud water and rain water were substantially larger than those of the parent cell, and there were also large number distributions from the ground to the 0 °C layer.

Figure 6 shows that the non-inductive charging regions of both the parent cell and the child cell were between the 0 and −40 °C layers in the updraft zone with a liquid water content of >0.2 g/kg. The non-inductive charging rate exhibited the characteristics of negative at the top and positive at the bottom, and the charging rate in the positive center was equal to that in the negative center. Together with consideration of Figure 5, it is evident that this region was also largely the center of the graupel. At this time, in the parent cell, the horizontal range in the updraft zone where the liquid water content was >0.2 g/kg was narrower. This means that although the distribution range, number concentration of the center, and the mixing ratio of the ice-phase particles of the parent cell were much wider than those of the child cell, the non-inductive charging zone of the parent cell was narrower than that of the child cell. The large vertical shear of the horizontal wind in the parent cell resulted in the tilting of the cloud and the notable horizontal variation in the cloud water content in the same direction. In the non-inductive S91 scheme, the inversion temperature was a function of the effective liquid water content and a skewed distribution of the inversion temperatures resulted in a skewed distribution of the charging zones. The vertical shear of the horizontal wind of the child cell was small, such that the cloud body was largely vertical, the inversion temperature was broadly distributed horizontally, and the non-inductive charging zone was stratified uniformly in the vertical direction.

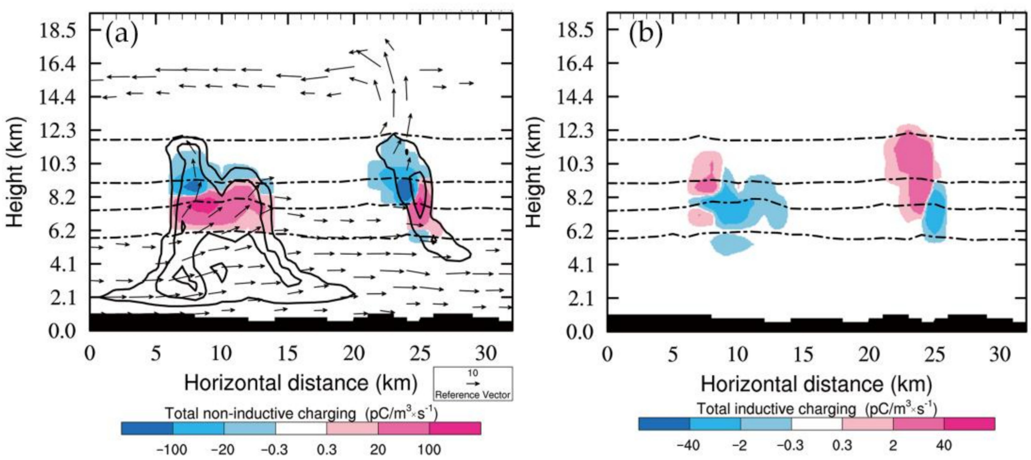

Figure 6. At 8:54, the non-inductive charging rate (**a**) and inductive charging rate (**b**) (the units are both pC/m^3 × s^{-1}), cloud water mixing ratio (black solid lines are 0.2, 0.8, and 1.5 g/kg from the outside to the inside, respectively), wind speed (vector arrows in m/s, larger than the superimposed horizontal and vertical wind speeds of 10 m/s), and isotherms distribution (black dashed lines are 0, −10, −20, and −40 °C from bottom to top, respectively) along the profile shown by the black profile line in Figure 3a.

The effects of the inductive charging processes are only obvious when a strong electric field is generated by the non-inductive charging processes [38]. Therefore, the distribution of the inductive and non-inductive charging zones of both the parent and the child cells were broadly the same, the polar distribution of the non-inductive charging rate was the opposite to that of the inductive charging rate, the non-inductive charging rate showed a negative top and positive bottom, and the inductive charging rate showed a positive top and negative bottom. The inductive charging rate was slightly lower in magnitude compared with that of the non-inductive charging rate. Consequently, it is confirmed that the role of the induction process cannot be ignored.

In the non-inductive charging mechanism, the charge polarity of large and small ice particles in the mixed-phase region was the opposite upon collision and separation, with large ice particles such as graupel and hail positively charged and small ice particles such as ice and snow negatively charged above the inversion temperature, and vice versa below the inversion temperature [35]. In Figure 7, the graupel and hail in the parent and child cells showed a negative top and positive bottom charging structure. Although the horizontal range of the non-inductive charging region of the parent cell was narrower than that of the child cell at this time (Figure 6), the distribution range of the graupel and hail was substantially larger than that of the child cell. This was because of the continued development of convection and the emergence of severe updrafts in the upper-middle parts of the cloud in the early stage of the parent cell (Figure 5). Therefore, the range and the density of the negative charges of the graupel and hail above the inversion temperature layer were markedly larger than those of the child cell. Owing to the narrow charging region in the middle-lower parts of the parent cell and the weak updraft, both the horizontal scale and the vertical extension height of the positively charged graupel and hail below the inversion temperature layer of the parent cell were smaller than those of the child cell.

For the same reason, the horizontal/vertical extents and the density of the positively charged ice and snow above the inversion temperature layer of the parent cell were notably larger than those of the child cell. Below the inversion temperature layer, the horizontal/vertical extents and the density of the negatively charged ice and snow of the parent cell were substantially smaller than those of the child cell. The ice crystals at the top updraft zone of the parent cell and in its anvil above -40 °C at the periphery of the updraft zone were negatively charged and widely distributed (Figures 5a and 7a). This was attributable to the inductive charging process making the cloud water negatively charged, which was homogeneously nucleated to form negatively charged ice after the strong updraft in the upper part of the parent cell transported it above the -40 °C layer. At this time, the severe horizontal airflow in the upper part of the parent cell meant that large quantities of negatively charged ice and positively charged snow were transported above the top of the child cell, which resulted in considerable amounts of negatively charged ice and positively charged snow appearing above the top of the child cell.

The charge structure of the cloud water in the child cell and the parent cell were basically consistent with those of the ice and snow, suggesting that the cloud droplets in this range were mainly formed by the melting of positively and negatively charged ice and snow. Different from that in the child cell, the cloud water in the upper part of the parent cell also had a negative charge area that was mainly formed by the inductive charging mechanism (Figure 6b). Raindrops were not directly involved in the electrification process, but the charge of the raindrops matched the polarity of the charge at the bottom of the graupel. Therefore, it can be determined that the charged raindrops were formed from the melting charged graupel.

In summary, through consideration of Figure 4a, Figure 5, and Figure 7, it can be determined that the different life stages of the parent and child cells meant that their vertical shear of the horizontal winds, hydrometeor numbers, charged numbers, and the charged polarities of their hydrometeors were different and caused obvious differences in the characteristics of the charge structure between the two cells. Overall, cloud water, ice, snow, and graupel in the parent–child cell were the main charged hydrometeors, whereas the raindrops and hail carried little charge. The charge structure during the feeder-type cells merging process was complex and cannot be described by the classical tripolar and bipolar charge structure [40].

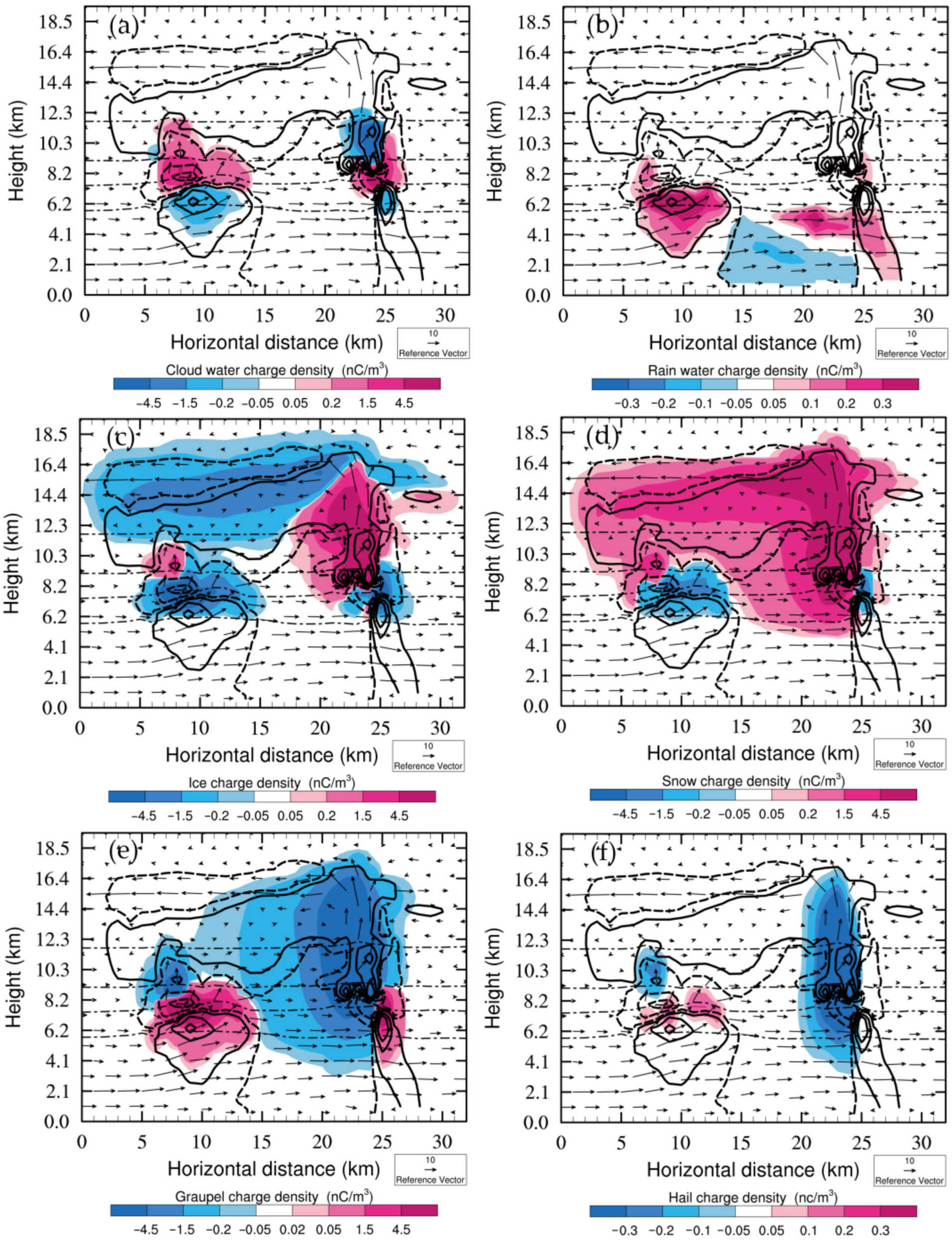

Figure 7. At 8:54, charge density of hydrometeors (colored shading in nC/m^3), total space charge density (black isopleths in nC/m^3, solid lines are positive, dashed lines are negative, values are $\pm$0.05, $\pm$0.25, $\pm$0.45 from the outside to the inside, respectively), wind speed (vector arrows in m/s, superimposed horizontal and vertical wind speeds), and distribution of isotherms (black contours are 0, $-$10, $-$20, and $-$40 °C from bottom to top, respectively) on the profile shown by black profile line in Figure 3a. ((**a**). Cloud, (**b**). rain, (**c**). ice, (**d**). snow, (**e**). graupel, (**f**). hail).

3.4. Distribution and Charging Characteristics of Hydrometeors in the Mid-Merger Period

In the mid-merger period, the parent cell was in the early extinction stage and the child cell was in the early mature stage (Figure 8). The number concentration and the mixing ratio of the ice in the upper part of the parent cell were diminished, whereas those in the upper part of the updraft of the child cell were markedly increased. The snow in the parent cell was mainly distributed in the upper part of the center of the cloud, whereas the snow in the child cell was distributed in the anvil of the cloud at the periphery of the updraft zone. The updraft in the upper part of the child cell was the strongest, and it was a zone with evident low values of snow number concentration and snow mixing ratio. The distribution of the graupel number concentration and the graupel mixing ratio indicate that the riming process was enhanced in the strong updraft zone, forming large numbers of graupel and consuming snow. The graupel and hail number concentrations and mixing ratios were much lower than those of the child cell.

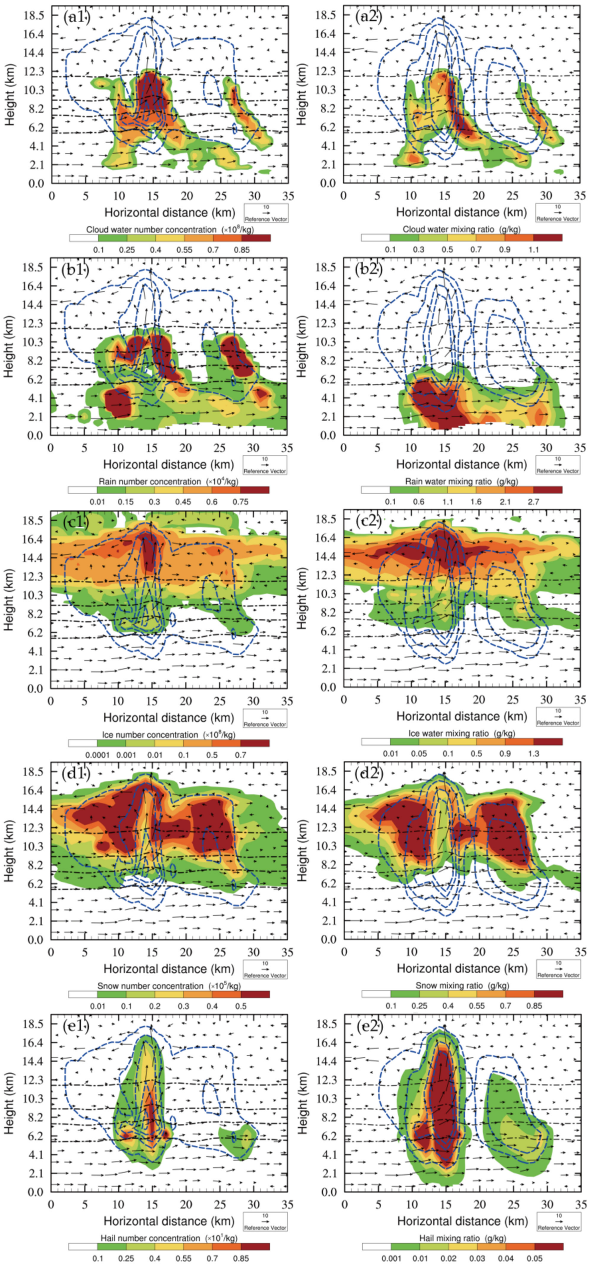

Figure 8. At 9:12, the number concentration (**a1**–**e1**) and mixing ratio (**a2**–**e2**) of hydrometeors, flow field (vector arrows in m/s, superimposed horizontal and vertical wind speeds), number concentration of graupel (blue dashed isopleths in the left column are 0.1, 0.7, 1.3, 1.9, and 2.5 ($\times 10^3$/kg) from the outside to the inside, respectively), mixing ratio of graupel (blue dashed isopleths in the right column are 0.1, 0.5, 2.0, and 3.5 g/kg from the outside to the inside, respectively) and isotherms distribution (black dashed lines are 0, −10, −20, and −40 °C from bottom to top, respectively) along the profile shown by the black profile line in Figure 3c. ((**a**). Cloud, (**b**). rain, (**c**). ice, (**d**). snow, (**e**). hail).

Compared with the conditions at 08:54 (Figure 5a,b), the number concentration and mixing ratio of the cloud water of the parent cell were reduced further. The number concentration of the rain water did not change much, but the rain water mixing ratio decreased slightly, indicating that the volume of raindrops was reduced. The number of droplets in the child cell increased slightly and its mixing ratio decreased, indicating reduced droplet size, which was attributable to the increased number of ice-phase particles that consume the cloud droplets via the condensation process between solid and liquid particles. The number concentration and mixing ratio of rain water of the child cell changed little. At this time, because the cloud anvil of the parent cell was no longer obvious, the large-value region of the rain water number concentration at the bottom connection between the parent and child cells disappeared, and this large-value region was mainly formed by the melting ice, snow, and graupel in the cloud anvil at the periphery of the updraft zone of the parent cell.

At this time, there were more ice-phase particles in the child cell than in the parent cell, which favored the non-inductive charging process in the child cell. The distributional characteristics of the inductive and non-inductive charging zones of the parent and child cells were the same as those before the merger (Figures 6 and 9), but the inductive and non-inductive charging rates of the child cell were markedly higher than those of the parent cell.

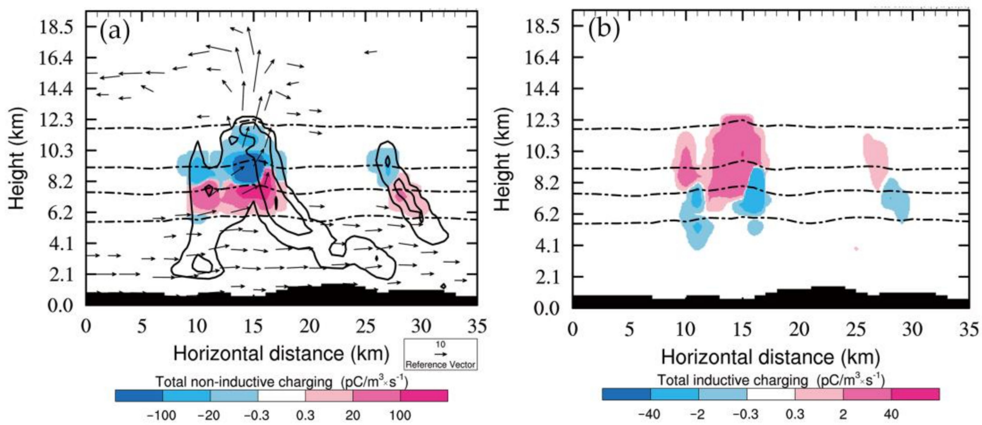

Figure 9. At 9:12, the non-inductive charging rate (**a**) and inductive charging rate (**b**) (the units are both $pC/m^3 \times s^{-1}$), cloud water mixing ratio (black solid lines are 0.2, 0.8, and 1.5 g/kg from the outside to the inside, respectively), wind speed (vector arrows in m/s, larger than the superimposed horizontal and vertical wind speeds of 10 m/s), and isotherms distribution (black dashed lines are 0, −10, −20, and −40 °C from bottom to top, respectively) along the profile shown by the black profile line in Figure 3c.

Figure 10 clearly shows that both the graupel of the parent cell and the hail of the child cell had a top-negative–bottom-positive charge structure. The amount of hail in the parent cell was small and therefore the associated charge could be ignored. The range and density of the negatively charged graupel and hail in the child cell increased substantially. The distributions of the charging range and density of ice and snow in the parent and child cells were the same as those of graupel, but the charge polarity of the ice and snow was the opposite to that of the graupel. Negatively charged ice was present in both the parent cell and the child cell above −40 °C, formed by the homogeneous nucleation and freezing of negatively charged cloud droplets.

Compared with the pre-merger period (Figure 7a,b), the overall charge structure of the cloud water of the parent cell was unchanged but the charge density decreased. The cloud water of the child cell shows a lower-negative–middle-positive–upper-negative tripolar charge structure. It reflected the appearance of negatively charged cloud water in the upper part of the child cell attributable to the markedly enhanced positive inductive charging rate in the child cell, which played a major role in producing the negatively charged cloud water in this zone. The rain water number concentration and rain water mixing ratio of the parent and child cells changed little (Figure 8) and therefore the charging characteristics of the rain water did not change substantially.

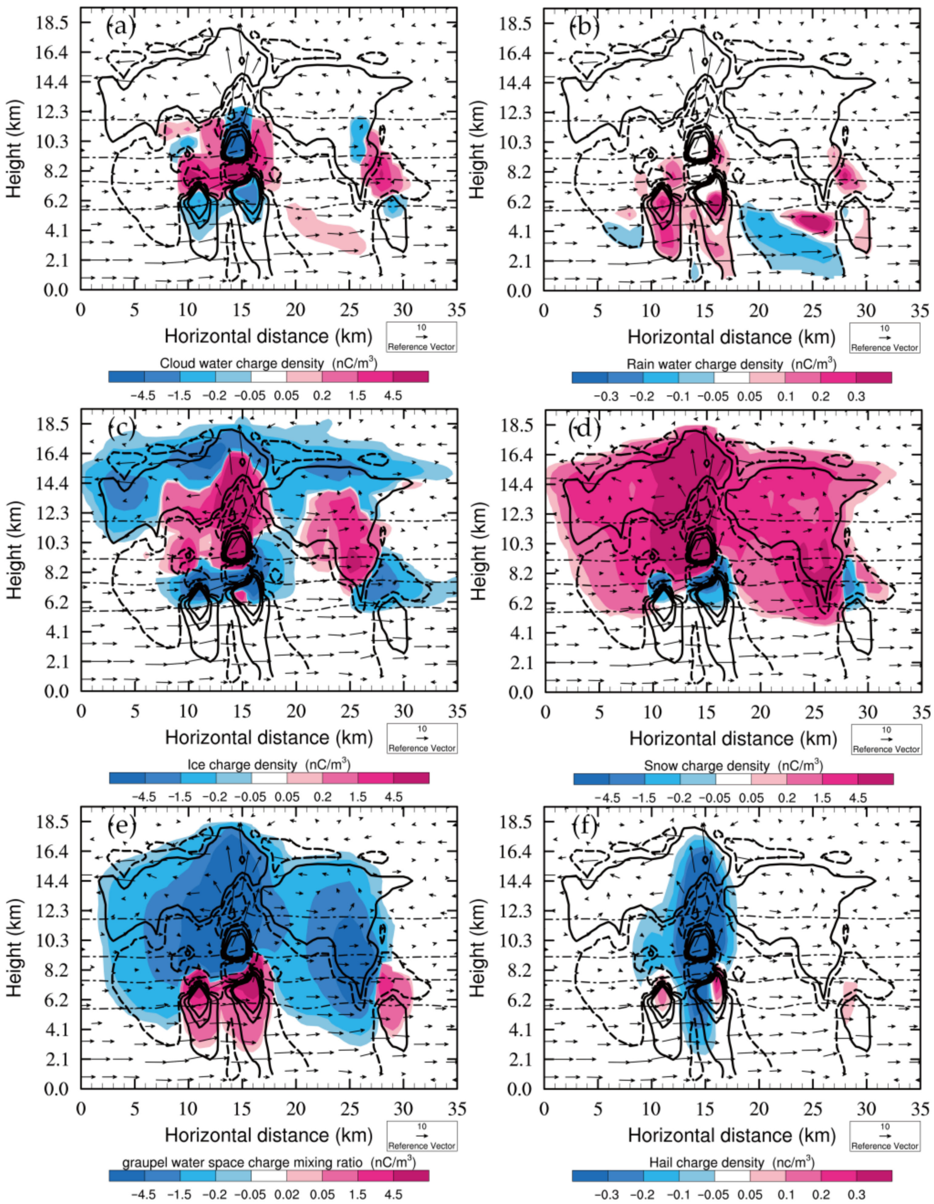

Figure 10. At 9:12, charge density of hydrometeors (colored shading in nC/m^3), total space charge density (black isopleths in nC/m^3, solid lines are positive, dashed lines are negative, values are ±0.05, ±0.25, ±0.45 from the outside to the inside, respectively), wind speed (vector arrows in m/s, superimposed horizontal and vertical wind speeds), and distribution of isotherms (black contours are 0, −10, −20, and −40 °C from bottom to top, respectively) on the profile shown by black profile line in Figure 3c. ((**a**). Cloud, (**b**). rain, (**c**). ice, (**d**). snow, (**e**). graupel, (**f**). hail).

Compared with the pre-merger period (Figure 7a,b), the charge structure of the child cell evolved from a lower-positive–middle-negative structure without an upper main positively charged region (P–N) to a six-layer (P–N–P–N–P–N) charge structure. The main region of positive charge at the altitude of 9–11 km and the upper region of positive charge at 14–17 km were newly generated and were dominated by positively charged ice and snow. Additionally, a new region of negative charge was generated at the altitude of 11–14 km, which was dominated by negatively charged graupel and hail. The thin layer of negative charge generated at the cloud top was dominated by negatively charged ice. The typical tripolar structure of the parent cell and the dominant particles in each charge region remained largely unchanged; however, the charge density was reduced. At this point in the merging process, the charge structure was complex.

3.5. Distribution and Charging Characteristics of Hydrometeors at the End of the Merger

Figure 11 clearly shows that the parent cell was in the late stage of extinction and that the child cell was in the late stage of maturity when the merger process was completed. In the parent cell, the number concentrations and mixing ratios of ice, snow, and graupel were very low, and little hail was evident. The number concentrations, mixing ratios, and distribution ranges of ice, snow, graupel, and hail in the child cell were decreased slightly compared to those in the mid-merger period (Figure 8).

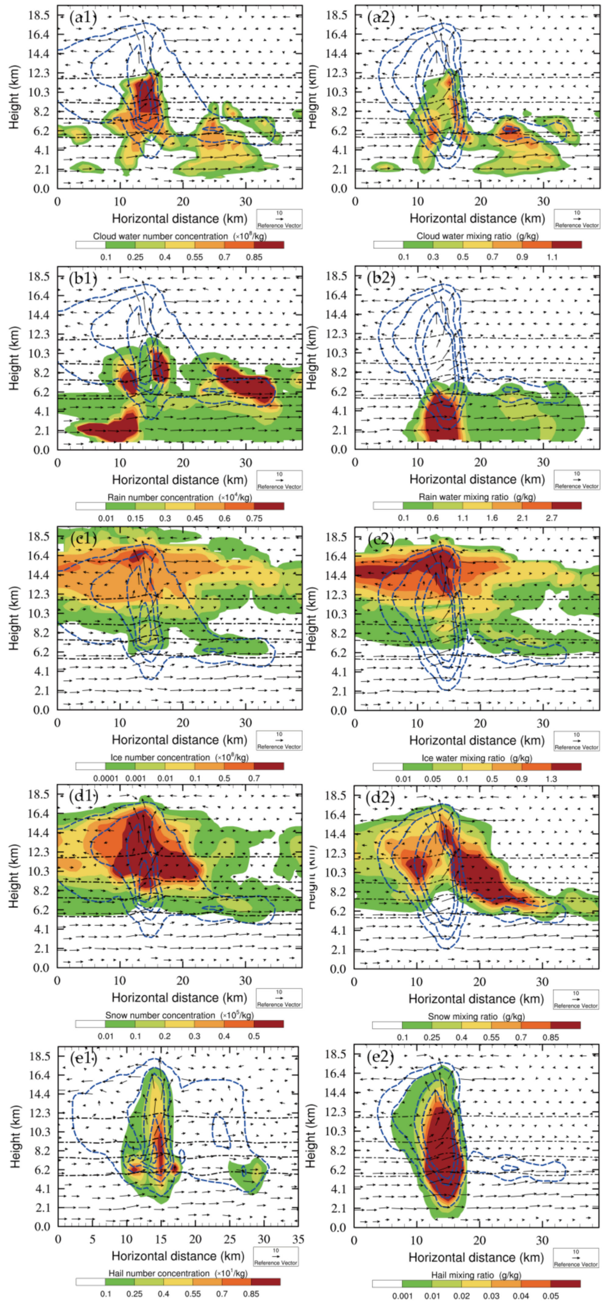

Figure 11. At 9:36, the number concentration (**a1**–**e1**) and mixing ratio (**a2**–**e2**) of hydrometeors, flow field (vector arrows in m/s, superimposed horizontal and vertical wind speeds), number concentration of graupel (blue dashed isopleths in the left column are 0.1, 0.7, 1.3, 1.9, and 2.5 ($\times 10^3$/kg) from the outside to the inside, respectively), mixing ratio of graupel (blue dashed isopleths in the right column are 0.1, 0.5, 2.0, and 3.5 g/kg from the outside to the inside, respectively), and isotherms distribution (black dashed lines are 0, −10, −20, and −40 °C from bottom to top, respectively) along the profile shown by the black profile line in Figure 3d. ((**a**). Cloud, (**b**). rain, (**c**). ice, (**d**). snow, (**e**). hail).

The number concentration and mixing ratio of the cloud water of the parent cell were both small and mainly distributed between the −10 °C layer and the ground. The number concentration of the rain water changed slightly but its mixing ratio decreased notably, indicating that the raindrop size was substantially reduced. The supply of warm humid air in the child cell was mostly cut off, the number concentration of the cloud water remained largely unchanged, but the cloud water mixing ratio was reduced, which means that the droplets were continuously consumed during the condensation process. The distribution of the number concentration and the mixing ratio of the rain water were similar to those in the mid-merger period (Figure 8b1,b2).

Figure 12 shows that the process of non-inductive charging in the parent and child cells remained strictly limited to the area where the cloud water content was >0.2 g/kg. In the late stage of extinction, the mixed-phase region of the parent cell with a cloud water content of >0.2 g/kg appeared only in a small range between the 0 and −10 °C layers, where a very weak positive non-inductive charging rate and a very weak negative inductive charging rate were evident. Compared with the merger period (Figure 9), the negative non-inductive charging rate, positive inductive charging rate, and their charging regions in the upper part of the child cell increased. Conversely, the positive non-inductive charging rate, negative inductive charging rate, and their charging regions in the lower part decreased.

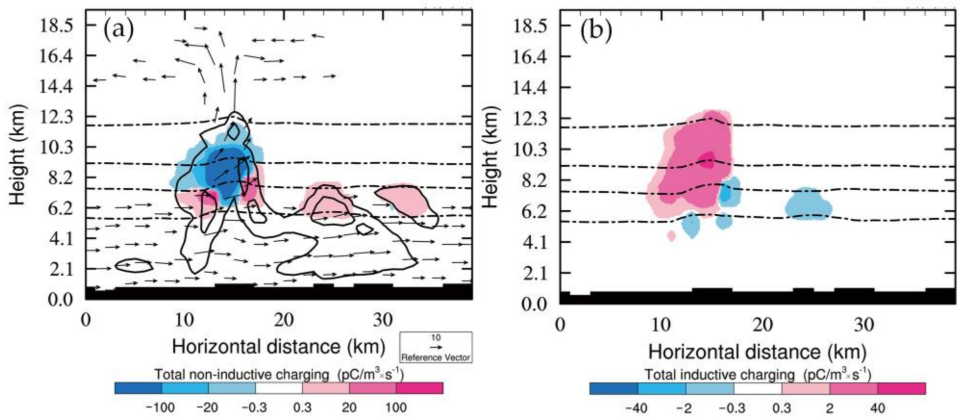

Figure 12. At 9:36, the non-inductive charging rate (**a**) and inductive charging rate (**b**) (the units are both $pC/m^3 \times s^{-1}$), cloud water mixing ratio (black solid lines are 0.2, 0.8, and 1.5 g/kg from the outside to the inside, respectively), wind speed (vector arrows in m/s, larger than the superimposed horizontal and vertical wind speeds of 10 m/s), and isotherms distribution (black dashed lines are 0, −10, −20, and −40 °C from bottom to top, respectively) along the profile shown by the black profile line in Figure 3d.

Figure 13 shows that the height of the charge regions of ice, snow, and graupel in the parent cell further decreased, the negatively charged ice dispersed in the parent cell above the −40 °C layer. There was no charged hail and therefore the positively and negatively charged ice and snow melted to form charged cloud water. At this time, the charge structure of the ice-phase particles in the child cell was similar to that during the merger (Figure 10), the distribution range and charge density of the upper negatively charged cloud water increased substantially, and the negatively charged cloud water was homogeneously nucleated to form negatively charged ice above the −40 °C layer under the effect of the updraft. The charge situation of the rain water in both the parent cell and the child cell was similar to that during the merger.

The tripolar charge structure of the parent cell was largely dissipated compared with that during the merger period (Figures 4d and 13), whereas the five-layer (P–N–P–N–P) charge structure of the child cell was mostly unchanged. The conclusion that can be drawn by considering Figures 10 and 13 is that due to the numbers of ice-phase particles at the height of both the upper region of positive charge and the main region of positive charge in the child cell were increased, where the growth in the numbers of positively charged ice and snow was much greater than that of the negatively charged graupel and hail. The overall performance showed positive polarity after superposition such that the charge density of the region increased. The numbers and distribution ranges of the positively charged graupel and hail at the bottom decreased compared with those in the merger period; thus, the overall charge density of the positive charge region at the bottom decreased. The thin layer of negative charge at the top of the cloud weakened, mainly because of the slight reduction in the negatively charged ice at the cloud top.

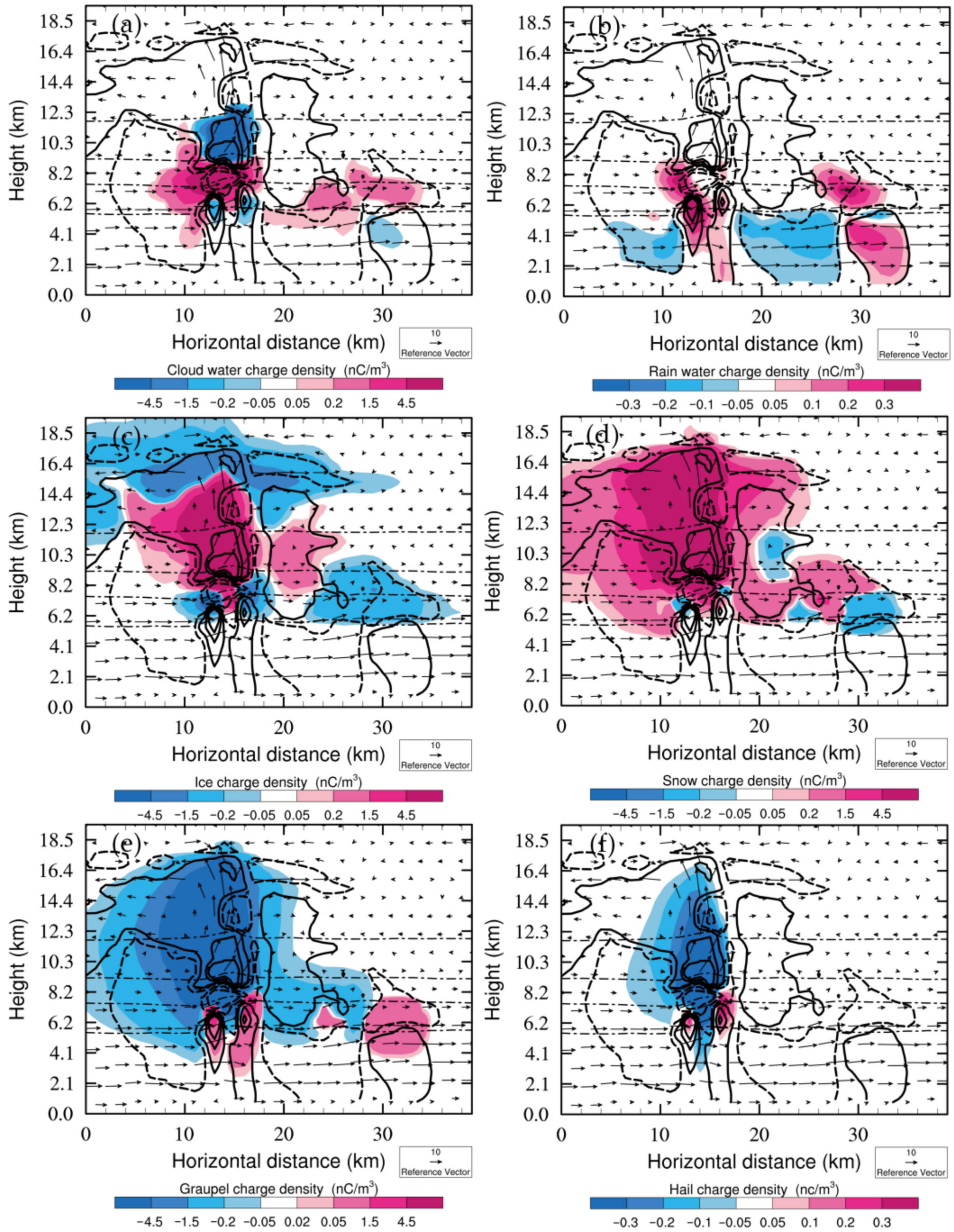

Figure 13. At 9:36, charge density of hydrometeors (colored shading in nC/m^3), total space charge density (black isopleths in nC/m^3, solid lines are positive, dashed lines are negative, values are ±0.05, ±0.25, ±0.45 from the outside to the inside, respectively), wind speed (vector arrows in m/s, superimposed horizontal and vertical wind speeds), and distribution of isotherms (black contours are 0, −10, −20, and −40 °C from bottom to top, respectively) on the profile shown by black profile line in Figure 3d. ((**a**). Cloud, (**b**). rain, (**c**). ice, (**d**). snow, (**e**). graupel, (**f**). hail).

4. Conclusions

This study used the WRF model with electrification and discharge parameterization schemes to simulate a feeder-type cells merging process that occurred at the tail of a squall line over Hubei Province on 27 June 2020. The following conclusions were derived through analysis of the relationships between the characteristics of the evolution of the total space charge density and the cloud dynamical–microphysical processes during the merging process of the two convective cells.

(1) The two cells in the feeder-type cells merging process were at different life stages. Initially, the parent cell was in the mature stage, and its upper part produced a divergent outflow that caused low-level convergence in its vicinity that stimulated the generation of the child cell. With the development of the child cell, the lower parts of the two cells gradually approached each other under the effect of the horizontal pressure gradient force, and the 30 dBZ echo connected to form a cloud bridge, indicating that the merger had begun. Subsequently, the child cell strengthened as the parent cell gradually weakened, and the strong echo core gradually tended to merge.

(2) The non-inductive charging zone in the cell was strictly limited to the mixed-phase region (between the 0 and -40 °C layers) with cloud water content > 0.2 g/kg in the updraft zone, and the distribution of charging rate mainly depended on the distribution of graupel. The effects of inductive charging processes were only obvious when a strong electric field was generated by non-inductive charging processes. Therefore, the distribution of the inductive charging zone of both the parent cell and the child cell was broadly similar to that of the non-inductive charging zone. The magnitude of the inductive charging rate was slightly smaller than that of the non-inductive charging rate. Generally, the importance of the inductive charging mechanism cannot be ignored.

(3) Both the parent cell and the child cell underwent this evolution of the charge structure. The cells showed a lower-positive–middle-negative (P–N) charge structure at the beginning of the development. With further development of the cell, the charge structure in the updraft zone developed into a six-layer (P–N–P–N–P–N) structure. With the emergence of a divergent outflow from the upper part of the cell, the uppermost thin layer of negative charge was transported by the divergent outflow toward the cloud anvil, leaving a charge structure of only five layers (P–N–P–N–P) in the updraft zone. As the cell continued to develop, the charge structure presented the typical tripolar (P–N–P) characteristic, followed by an overall reduction in the height of each charge region and weakening of the charge density until the cell dissipated. The charge region at the periphery of the updraft zone appeared after the maturation period of the cell, and manifested as a three-layer (N–P–N) structure from the bottom to the top.

(4) In the merging process, overall, the cloud droplets, ice, snow, and graupel in the cell were the main charged hydrometeors, whereas rain and hail had little charge. The parent and child cells were always in different life stages. The vertical shear of the horizontal winds differed in each cell, and there were differences in the content, charge number, and charge polarity of the hydrometeors, resulting in obvious differences in the characteristics of the charge structure between the two cells. Therefore, the combined cells had a complex charge structure that cannot be described by the classical tripolar and bipolar charge structures.

This study analyzed a feeder-type cells merging process, focusing on the relationships between the dynamical–microphysical processes and the characteristics of the evolution of the charge structure. However, the analysis did not consider the lightning characteristics. Moreover, the question of whether the studied cells merging process is universally representative remains to be confirmed by further research. Additional observational data and more case studies should be considered to provide a more generalized understanding in the future.

Author Contributions: J.D.: conceptualization, draft syllabus, investigation, data collation and validation, visualization and interpretation, analysis, write-up and proofreading; F.G.: conceptualization, analysis, data interpretation, write-up, review and editing; J.S.: conceptualization and collecting primary data; Z.W. and Z.L.: suggestions about running WRF model; X.L., K.C. and Q.W.: proofreading. All authors have read and agreed to the published version of the manuscript.

Funding: This work was supported by the National Natural Science Foundation of China (41975003), the Natural Science Foundation of Hubei Province, China (2021CFB571), and the Second Tibetan Plateau Scientific Expedition (2019QZKK0104).

Institutional Review Board Statement: Not applicable.

Informed Consent Statement: Statement not applicable.

Data Availability Statement: The data presented in this study are available on request from the corresponding author. The data are not publicly available due to the data also forms part of an ongoing study.

Acknowledgments: We appreciate the National Centers for Environmental Prediction for providing the FNL reanalysis data. We also appreciate the computer resources at the NUIST High Performance Computer Center. Thanks for the use of the WRF preprocessor tool.

Conflicts of Interest: The authors declare no conflict of interest.

References

1. Westcott, N.E. Merging of Convective Clouds: Cloud Initiation, Bridging, and Subsequent Growth. *Mon. Weather Rev.* **1994**, *122*, 780–790. [CrossRef]
2. Knievel, J.C.; Johnson, R.H. The Kinematics of a Midlatitude, Continental Mesoscale Convective System and Its Mesoscale Vortex. *Mon. Weather Rev.* **2002**, *130*, 1749–1770. [CrossRef]
3. Pozo, D.; Borrajero, I.; Marín, J.C.; Raga, G.B. A Numerical Study of Cell Merger over Cuba; Part II: Sensitivity to Environmental Conditions. *Ann. Geophys.* **2006**, *24*, 2793–2808. [CrossRef]
4. Shen, F.; Xu, D.; Li, H.; Liu, R. Impact of Radar Data Assimilation on a Squall Line over the Yangtze–Huaihe River Basin with a Radar Reflectivity Operator Accounting for Ice-phase Hydrometeors. *Meteorol. Appl.* **2021**, *28*, e1967. [CrossRef]
5. Shen, F.; Song, L.; He, Z.; Xu, D.; Chen, J.; Huang, L. Impacts of adding hydrometeor control variables on the radar reflectivity data assim-ilation for the 6–8 August 2018 mesoscale convective system case. *Atmos. Res.* **2023**, *295*, 107012. [CrossRef]
6. Tao, W.-K.; Simpson, J. Cloud Interactions and Merging: Numerical Simulations. *J. Atmos. Sci.* **1984**, *41*, 2901–2917. [CrossRef]
7. Kogan, Y.L.; Shapiro, A. The Simulation of a Convective Cloud in a 3D Model with Explicit Microphysics. Part II: Dynamical and Microphysical Aspects of Cloud Merger. *J. Atmos. Sci.* **1996**, *53*, 2525–2545. [CrossRef]
8. Lee, B.D.; Jewett, B.F.; Wilhelmson, R.B. The 19 April 1996 Illinois Tornado Outbreak. Part II: Cell Mergers and Associated Tornado Incidence. *Weather Forecast.* **2006**, *21*, 449–464. [CrossRef]
9. Gauthier, M.L.; Petersen, W.A.; Carey, L.D. Cell Mergers and Their Impact on Cloud-to-Ground Lightning over the Houston Area. *Atmos. Res.* **2010**, *96*, 626–632. [CrossRef]
10. Yi, X.; Sun, X.; Zhang, Y.; Guo, L.; Wang, Y. Evolution of radar parameters and lightning activity during thunderstorm cells merging. *Acta Meteorol. Sin.* **2017**, *75*, 981–995.
11. Lu, J.; Qie, X.; Jiang, R.; Xiao, X.; Liu, D.; Li, J.; Yuan, S.; Chen, Z.; Wang, D.; Tian, Y.; et al. Lightning Activity during Convective Cell Mergers in a Squall Line and Corresponding Dynamical and Thermodynamical Characteristics. *Atmos. Res.* **2021**, *256*, 105555. [CrossRef]
12. Lu, J.; Qie, X.; Xiao, X.; Jiang, R.; Mansell, E.R.; Fierro, A.O.; Liu, D.; Chen, Z.; Yuan, S.; Sun, M.; et al. Effects of Convective Mergers on the Evolution of Microphysical and Electrical Activity in a Severe Squall Line Simulated by WRF Coupled with Explicit Electrification Scheme. *J Geophys. Res.-Atmos.* **2022**, *127*, e2021JD036398. [CrossRef]
13. Huang, M.; Xu, S.; Ji, W. Numerical simulation study of cumulus merging and interaction. *Sci. Sin.* **1987**, *17*, 214–224.
14. Fu, D.; Guo, X. The Role of Cumulus Merger in a Severe Mesoscale Convective System. *Chin. J. Atmos. Sci.* **2007**, *31*, 635–644.
15. Li, Y.; Niu, S.; Yao, Z.; Luo, N.; Wen, J.; Huang, H. Initial part discussion of cloud merger. *Chin. J. Atmos. Sci.* **2009**, *33*, 1015–1026.
16. Zhai, J.; Hu, W.; Feng, Y.; Huang, Y. Numerical simulations of convective cloud merging processes at different development stages. *Chin. J. Atmos. Sci.* **2012**, *36*, 697–712.
17. Zhai, J.; Huang, Y.; Hu, W.; Jiang, N.; Mou, R. Observation and analysis on cumulus merging in severe mesoscale convective system. *Sci. Meteorol. Sin.* **2011**, *31*, 100–106.
18. Yi, X.; Zhang, Y.; Wang, H.; Dong, H.; Zhang, N.; Xu, S. Characterizes on Evolution of the Heavy Rainfall Cells Structure in the Leading Line Meso-scale Convective System and Lightning Activity. *Acta Meteorol. Sin.* **2013**, *71*, 1035–1046.
19. Wang, A.; Zhao, X. The merging of clouds and formation of hailcloud. *Acta Meteorol. Sin.* **1983**, *41*, 204–210. [CrossRef]
20. Yi, X.; Zhang, Y.; Shen, Y.; Liu, Y.; Sun, X. Observational analysis of a multicell hailstorm triggered by a sea-breeze front and its merging process. *Acta Meteorol. Sin.* **2012**, *70*, 974–985.

21. Dennis, A.S.; Schock, C.A.; Koscielski, A. Characteristics of Hailstorms of Western South Dakota. *J. Appl. Meteor.* **1970**, *9*, 127–135. [CrossRef]
22. Bringi, V.N.; Knupp, K.; Detwiler, A.; Liu, L.; Caylor, I.J.; Black, R.A. Evolution of a Florida Thunderstorm during the Convection and Precipitation/Electrification Experiment: The Case of 9 August 1991. *Mon. Weather Rev.* **1997**, *125*, 2131–2160. [CrossRef]
23. Knupp, K.R.; Geerts, B.; Goodman, S.J. Analysis of a Small, Vigorous Mesoscale Convective System in a Low-Shear Environment. Part I: Formation, Radar Echo Structure, and Lightning Behavior. *Mon. Weather Rev.* **1998**, *126*, 1812–1836. [CrossRef]
24. Carey, L.D.; Rutledge, S.A. The Relationship between Precipitation and Lightning in Tropical Island Convection: A C-Band Polarimetric Radar Study. *Mon. Weather Rev.* **2000**, *128*, 2687–2710. [CrossRef]
25. Feng, G.; Qie, X.; Yuan, T.; Niu, S. Lightning Activity and Precipitation Structure of Hailstorms. *Sci. Sin.* **2007**, *50*, 629–639. [CrossRef]
26. MacGorman, D.R.; Filiaggi, T.; Holle, R.L.; Brown, R.A. Negative Cloud-to-Ground Lightning Flash Rates Relative to VIL, Maximum Reflectivity, Cell Height, and Cell Isolation. *J. Light. Res.* **2007**, *1*, 132–147.
27. Cheng, Q.; Zhang, K.; Xia, Y.; Liu, J.; Tang, M. Analysis of relationship between lightning and rainfall during "6·27" super rainstorm of Hubei Province in 2020. *Torrential Rain Disasters* **2020**, *39*, 620–628.
28. Mansell, E.R.; Ziegler, C.L.; Bruning, E.C. Simulated Electrification of a Small Thunderstorm with Two-Moment Bulk Microphysics. *J. Atmos. Sci.* **2010**, *67*, 171–194. [CrossRef]
29. Ziegler, C.L. Retrieval of Thermal and Microphysical Variables in Observed Convective Storms. Part 1: Model Development and Preliminary Testing. *J. Atmos. Sci.* **1985**, *42*, 1487–1509. [CrossRef]
30. Takahashi, T. Riming Electrification as a Charge Generation Mechanism in Thunderstorms. *J. Atmos. Sci.* **1978**, *35*, 1536–1548. [CrossRef]
31. Saunders, C.P.R.; Peck, S.L. Laboratory Studies of the Influence of the Rime Accretion Rate on Charge Transfer during Crystal/Graupel Collisions. *J. Geophys. Res.* **1998**, *103*, 13949–13956. [CrossRef]
32. Berdeklis, P.; List, R. The Ice Crystal–Graupel Collision Charging Mechanism of Thunderstorm Electrification. *J. Atmos. Sci.* **2001**, *58*, 2751–2770. [CrossRef]
33. Saunders, C.P.R.; Bax-norman, H.; Emersic, C.; Avila, E.E.; Castellano, N.E. Laboratory Studies of the Effect of Cloud Conditions on Graupel/Crystal Charge Transfer in Thunderstorm Electrification. *Q. J. R. Meteorol. Soc.* **2006**, *132*, 2653–2673. [CrossRef]
34. Fierro, A.O.; Mansell, E.R.; MacGorman, D.R.; Ziegler, C.L. The Implementation of an Explicit Charging and Discharge Lightning Scheme within the WRF-ARW Model: Benchmark Simulations of a Continental Squall Line, a Tropical Cyclone, and a Winter Storm. *Mon. Weather Rev.* **2013**, *141*, 2390–2415. [CrossRef]
35. Helsdon, J.H.; Wojcik, W.A.; Farley, R.D. An Examination of Thunderstorm-Charging Mechanisms Using a Two-Dimensional Storm Electrification Model. *J. Geophys. Res.* **2001**, *106*, 1165–1192. [CrossRef]
36. Saunders, C.P.R.; Keith, W.D.; Mitzeva, R.P. The Effect of Liquid Water on Thunderstorm Charging. *J. Geophys. Res.* **1991**, *96*, 11007. [CrossRef]
37. Mansell, E.R. Charge Structure and Lightning Sensitivity in a Simulated Multicell Thunderstorm. *J. Geophys. Res.* **2005**, *110*, D12101. [CrossRef]
38. Ziegler, C.L.; MacGorman, D.R.; Dye, J.E.; Ray, P.S. A Model Evaluation of Noninductive Graupel-Ice Charging in the Early Electrification of a Mountain Thunderstorm. *J. Geophys. Res.* **1991**, *96*, 12833. [CrossRef]
39. MacGorman, D.R.; Straka, J.M.; Ziegler, C.L. A Lightning Parameterization for Numerical Cloud Models. *J. Appl. Meteorol. Clim.* **2001**, *40*, 459–478. [CrossRef]
40. Williams, E.R. The Tripole Structure of Thunderstorms. *J. Geophys. Res.* **1989**, *94*, 13151–13167. [CrossRef]